

Angle-resolved polarized Raman spectroscopy for distinguishing stage-I graphite intercalation compounds with Thorium, Uranium and Plutonium

Kun Yan^{1 a)}

¹State Key Laboratory of Optoelectronic Materials and Technologies, Guangdong Province Key Laboratory of Display Material and Technology, School of Physics, Sun Yat-sen University, Guangzhou 510275, People's Republic of China.

^{a)}Correspondence: yank6@mail2.sysu.edu.cn

Abstract

Graphite intercalation compounds (GICs) with the geometrical anisotropy and strong electron-phonon coupling are in full swing and have shown their great potential for applications in nanodevices. I selected representative three elements in actinide group with valence electron arrangement: Thorium (Th) ([Rn]6d27s2), Uranium (U) ([Rn]5f36d17s2), Plutonium (Pu) ([Rn]5f67s2). I calculated their phonon spectra and demonstrated the atomic-scale microstructure identification of actinide graphite intercalation compounds by angle-resolved polarized Raman spectroscopy.

KEYWORDS

angle-resolved polarized Raman spectroscopy, graphite intercalation compounds, crystallographic orientation, nuclear fission elements

1 | Introduction

The synthesis of a graphite intercalation compound (GIC) was first reported by Schaffäutl (1841). Due to its unique electronic structure and Fermi surface, transport characteristics, optical spectra, magneto-optical phenomenon, magnetic susceptibility and magnetic resonance, specific heat, superconductivity, high conductivity ($5.8 \times 10^5 \text{ } (\Omega \text{ cm})^{-1}$, comparable to copper), lattice vibration modes, the GICs' potential is unlimited in the application of battery and electrodes, catalysis, , laser diodes, high-power devices, sensors, etc. Alkali and alkaline earth metals have been artificially intercalated into graphite sheets to achieve superconducting properties[1-3]. GICs of transition metal elements have also been partially studied, but due to the complexity of molecular orbitals and electronic structures, there has been no generally accepted and consistent conclusions/rules to be achieved. The GICs with lanthanide (Ln) and actinide (An) groups containing f-orbital electrons are even less studied. So far, only the similar η^6 -benzene or η^8 -cyclooctatetraene (COT) Ln and An complexes have been chemically synthesized[4]. Nevertheless, the Ln and An groups include extremely important elements, such as Thorium (Th), Uranium (U), Plutonium (Pu) and other raw materials for nuclear energy utilization. Furtherly, Th ($[\text{Rn}]6d^27s^2$) has valence electrons of only d and s orbit, Pu ($[\text{Rn}]5f^67s^2$) has (ones of) only f and s orbit, and U ($[\text{Rn}]5f^36d^17s^2$) has all.

Angle-resolved Photo-emission Spectroscopy (ARPES) is usually employed to explore the electronic properties of the GICs with alkali and alkaline earth metal elements. However, due to the anisotropy and strong electron-phonon coupling (EPC), as has been discovered, Angle-resolved Polarized Raman Spectroscopy (APRS) may be a fast, effective, and nondestructive alternative to fingerprint differences at the atomic scale within similar molecular structures[5-7].

In this work, I calculated the Phonon dispersion and Angle-resolved Polarized Raman Intensity (APRI) of stage-I GICs with Th, U and Pu. I discovered that the GICs are all dynamically stable. Thus, I further simulated the APRI of the six types with different metal elements and their various densities and distribution features. It is demonstrated that the sharp distinctions in APRI can be a clear and easy basis for identification of geometry and the

crystallographic orientation.

2 | Model and Methods

Six types of stage-I GICs with actinide (An) group metal elements Thorium (Th), Uranium (U) and Plutonium (Pu) were designed. ‘stage-I’ was experimentally reported[8] to have the strongest conductivity, just like monolayer graphene to which metal nanoparticles attach. It is explained by the strong EPC effect. The metal atoms are so large that 2-dimensional carbon layer is basically tiled by octagons and quadrilaterals[9] (see Fig. 1), and the metal atoms bond with carbons in the upper and lower octagons. After geometric optimization, the C-C bond length between two adjacent octagons is 1.44 Å; the C-C bond length between the quadrilateral and octagon is 1.48 Å. Those C-C bond lengths are consistent with previous research results[9], which notes the former as “short” ones and the latter as “long” ones. The distance between the upper and lower adjacent carbon layers ranges from 3.8 to 4.3 Å, according to the metal element and its density. When the metal atoms fill the middle of the octagon (so its density marks “100%”), such as 2DU100, the distance between adjacent U atoms is 3.45 Å. When the density of metal atoms is “50%”, as shown in Fig. 1(c), the distance between adjacent U atoms is 4.87 Å. Fig. 1(e) and (f) indicate 2 way of metal atom (e.g. U) distribution with the same density (“25%”), noted as 2DU25-1 and 2DU25-2. As I are focus on demonstrating the probability and reliability of APRI’s fingerprint, no more discussion of else density and distribution way is to be added in this paper.

Geometric optimization and electronic structure were carried out with density functional theory (DFT) as implemented in Vienna Ab initio simulation package (VASP) code. The exchange-correlation potential was treated at the level of generalized gradient approximation (GGA) using Perdew–Burke–Ernzerh of (PBE) functionals. A plane-wave energy cutoff of 480 eV was employed in all calculations. The force and electronic convergence tolerance were set to 10^{-5} eV/Å and 10^{-6} eV, respectively in the full geometrical optimizations. The k-point grid was set to $8 \times 8 \times 4$ in structure optimization. Spin polarization was performed and due to the localized *d*- and *f*-orbital electrons a GGA+U approach was used in all calculations. The vibrational frequencies

and eigenvectors of phonons were obtained with Phonopy code [10]. $2 \times 2 \times 2$ supercells were chosen in phonon calculations.

The Raman scattering cross section of the Stokes part per unit cell is [11-19]

$$\frac{d\sigma_v}{d\Omega} = V_0 \frac{(\omega_i - \omega_v)^4}{(4\pi)^2 c^4} \left| \vec{e}_s \cdot \vec{R}_v \cdot \vec{e}_i \right|^2 (n_v + 1) \frac{\hbar}{2\omega_v} \quad (1)$$

$$\vec{R}_{\alpha\beta}(\nu) = \sqrt{V_0} \sum_{\mu=1}^N \sum_{l=1}^3 \frac{\partial \chi_{\alpha\beta}}{\partial r_l(\mu)} \frac{e_l^\nu(\mu)}{\sqrt{M_\mu}} \quad (2)$$

where V_0 is the unit cell volume; ω_i and ω_v are the frequencies of the incident light and the ν -th vibrational mode, respectively; \vec{e}_s and \vec{e}_i are the polarization directions of the scattered light and the incident light, respectively; \vec{R}_v is the Raman tensor; n_v is the Bose factor; $\frac{\partial \chi_{\alpha\beta}}{\partial r_l(\mu)}$ is the first-order derivative of the frequency-dependent linear dielectric susceptibility tensor χ with respect to $r_l(\mu)$ (the displacement of the μ -th atom along direction l); $e_l^\nu(\mu)$ is the eigenvector of the ν -th phonon mode at Γ point; c is the light velocity in vacuum; \hbar is Reduced Planck Constant; M_μ is the molecular weight of the μ th atom.

3 | Results and discussion

3.1 | Phonon Dispersion

No imaginary value in the Phonon Dispersion means that all the six types of GICs have dynamic stability. That the spectra of 2DU25-1 and 2DU25-2 have more denser curves is because their unit cells have twice as many atoms as the other structures. The metal atoms are far larger and heavier than C atoms, so their projected density of states (PDOS) contribute to low frequency phonons.

3.2 | Angle-resolved polarized Raman spectroscopy (APRS) for distinction

Our calculation coincides with group theory (shown in Table 1). Thus, the Raman tensor can be written in a general form:

$$R = \begin{bmatrix} a & d & e \\ d & b & f \\ e & f & c \end{bmatrix} \quad (3)$$

The intensity of APRS (APRI) is calculated in a backscattering configuration, while the polarization of the scattered light can be perpendicular (\perp) or parallel (\parallel) to that of the incident light. When the k vector of the incident laser is in y direction ($\hat{k}_i \parallel y$) with polarization direction $\vec{e}_i = (\cos\theta, 0, \sin\theta)$, the polarization directions of scattered light in parallel and perpendicular configuration can be written as $\vec{e}_s^{\parallel} = (\cos\theta, 0, \sin\theta)$ and $\vec{e}_s^{\perp} = (-\sin\theta, 0, \cos\theta)$, respectively. That way can be used to study the interaction and EPC between the metal atoms and the carbon 2-dimentional network. When the k vector of the incident laser is in z direction ($\hat{k}_i \parallel z$) with polarization direction $\vec{e}_i = (\cos\theta, \sin\theta, 0)$, the polarization directions of scattered light in parallel and perpendicular configuration can be written as $\vec{e}_s^{\parallel} = (\cos\theta, \sin\theta, 0)$ and $\vec{e}_s^{\perp} = (-\sin\theta, \cos\theta, 0)$, respectively. That way can study the anisotropy in xy plane, and the various distribution feature of metal atoms.

Usually, in experiments we know the z-axis direction of the sample (using an optical microscope would be ok). Since the angle between the polarization direction of the incident light and the x-axis direction is set to an arbitrary θ , the x and y axis directions could be set arbitrary, just required to be in a plane perpendicular to the z axis. Thus we set the laboratory coordinates as shown in Figure 1(a) and (g).

Therefore, by substituting into formula (2) the above \vec{e}_i , \vec{e}_s and Raman tensor \vec{R} calculated with VASP according to formula (1), I have the intensity for the parallel-polarization configuration 1 when $\hat{k}_i \parallel y$:

$$I_{\hat{k}_i \parallel y}^{\parallel}(\theta) \propto \left| a \cdot \cos^2 \theta + c \cdot \sin^2 \theta + e \cdot \sin 2\theta \right|^2 \cdot \frac{(n_v + 1) \cdot \omega_i^4}{\omega_v} \quad (4)$$

and the cross-polarization configuration 2 when $\hat{k}_i \parallel y$:

$$I_{\hat{k}_i \parallel y}^{\perp}(\theta) \propto \left| \frac{(c-a)}{2} \cdot \sin 2\theta + e \cdot \cos 2\theta \right|^2 \cdot \frac{(n_v + 1) \cdot \omega_i^4}{\omega_v} \quad (5)$$

Similarly, I have the intensity for the parallel-polarization configuration 3 when $\hat{k}_i \parallel z$:

$$I_{\hat{k}_i \parallel z}^{\parallel}(\theta) \propto \left| a \cdot \cos^2 \theta + b \cdot \sin^2 \theta + d \cdot \sin 2\theta \right|^2 \cdot \frac{(n_v + 1) \cdot \omega_i^4}{\omega_v} \quad (6)$$

and the cross-polarization configuration 4 when $\hat{k}_i \parallel z$:

$$I_{\hat{k}_i \parallel z}^{\perp}(\theta) \propto \left| \frac{(b-a)}{2} \cdot \sin 2\theta + d \cdot \cos 2\theta \right|^2 \cdot \frac{(n_v + 1) \cdot \omega_i^4}{\omega_v} \quad (7)$$

Based on formulas (4) to (7), we obtained the APRI of the prominent peaks of the GICs (Fig. 2-5).

For 2DTh50, when $\hat{k}_i \parallel y$, there is a strong peak of 404 cm^{-1} mode for A_g in configuration 1 and 2,

and an obvious curve rotation of 307.5 cm^{-1} due to the non-negligible absorption of 633 nm light;

due to $|a| = |b| < |d|$, 1119.4 cm^{-1} mode has a particular shape in configuration 3 and a four-fold

symmetry with axis $\theta=0^\circ$ and $\theta=90^\circ$ in configuration 4. For B_g , the 1285.9 cm^{-1} mode is so

strong that it can be used to identify such structure. Also, the shape of the mode is like an ellipse

with the major axis twice the minor axis, due to $|a| \approx |b| \approx 2|d|$. Similar analysis can be applied to

other structures. For 2DPu50, the 1098.3 cm^{-1} mode and the 1099.9 cm^{-1} mode are highly strong

for identification in A_g . For 2DU50, the strong 1447 cm^{-1} mode has four-fold symmetry with axis

$\theta=0^\circ$ and $\theta=90^\circ$ in configuration 4 and a ‘‘asymmetric four petals’’ shape (due to

real part: $|a| \approx |b| \approx |d|$, imaginal part $\approx 1/10 \cdot \text{real part}$) in configuration 3. Also, the 306.4 cm^{-1}

mode has special shapes in both configuration 1 and 2 (due to $|a| \approx |e| \gg |c|$). Both features can be

used to identify 2DU50. If $|a| \approx |b| \gg |d|$, the shape is a circle and if $|a| \neq |b| \gg |d|$, an ellipse. If

$|d| \neq 0$, we attain a ‘‘spindle body’’ with $I \neq 0$ when $\theta=90^\circ$, which is the prominent feature for

2DU100 in configuration 1. There is no obvious rotation of APRI curves in 2DU100, due to the

possibly weak absorption of the relatively low frequencies of selected phonons. The 581.5 cm^{-1}

mode and 360.3 cm^{-1} mode in configuration 1 and 452.2 cm^{-1} mode in configuration 3 can be used

to identify 2DU25_1 due to their peculiar shape. The appearance of dense strong peaks with

various rotation in configuration 4 can be another basis for identification. For 2DU25_2, in

configuration 3 the curves all have an oval shape and in configuration 4 A_{1g} modes and B_{2g} modes

have four-fold symmetry with axis $\theta=0^\circ$ and $\theta=90^\circ$, which both are obviously different from 2DU25_1. I consider those can be used to distinguish 2DU25_1 and 2DU25_2.

Moreover, comparing the experimental results with the theoretical simulation above, I can easily confirm the configuration and furtherly the x/y/z-axis's direction. For example, the θ_0 can be determined by $\left. \frac{dI}{d\theta} \right|_{\theta_0} = 0$, where I takes extremum when $\theta=\theta_0$. Then since the x or y-axis' direction has been set to along $\theta=0^\circ$ or $\theta=90^\circ$ respectively, the crystallographic orientation can be determined, e.g. x axis, by rotating clockwise θ_0 the angle of symmetry axis of the APR curves based on our calculation.

3.3 | Some problems in experiment

Owing to the big size of the actinide metal atoms, the preparing method diffusing alkali and alkaline earth metals into graphite from the edge of the sheets is never applied. There are 2 probable routes for the preparation of the GICs in this work:

1. Using the means of thin film growth: By MOCVD, etc., add a layer of actinide metal atoms on the top of a layer of graphene, then cover the material with another layer of graphene, and then grow another metal layer...Thus, metal atomic layers and graphene are alternately stacked and grown layer by layer.

2. Using the hydrostatic pressure: The high pressure drives the metal atoms slowly pass through the carbon ring with relaxed structure and gradually enter the inner of graphite.

Like high-density solid-state hydrogen storage materials, reducing pressure or heating could release metals from GICs. Also, those GICs could be expected to be recycled.

There are other questions: what is the resolution needed to separate to neighboring lines? When a focusing lens is used to have a micron size laser beam, the laser beam is no more completely perpendicular to the surface; hence, zero Raman intensity cannot be observed: how does this effect modify the calculated Raman curve? Owing to the sample not yet prepared, the

lack of comparison between calculated curves and experimental results is a serious drawback. The author find a literature entitled “The high-resolution Raman spectroscopy of crystalline uranocene, thorocene, and ferrocene”[20]. I calculated the phonon spectra of those crystals again and found the imaginary frequency disappeared when I selected a correct/right U value (see Fig. S1). Also, the obtained frequencies are closer to the experimental (RUN) data than the DFT results in the literature (see Table S1). The deviation may stem/come from the ignorance of vdW correction.

4 | Conclusions

Graphite intercalation compounds (GICs) with unique physical properties are in full swing and have shown their great potential for applications in nanodevices. I selected representative three elements of/in actinide group with valence electron arrangement: Thorium (Th) ($[\text{Rn}]6d^27s^2$), Uranium (U) ($[\text{Rn}]5f^36d^17s^2$), Plutonium (Pu) ($[\text{Rn}]5f^67s^2$). I calculated their phonon spectra and demonstrated the atomic-scale microstructure identification of actinide graphite intercalation compounds by APRI. The phonon dispersions of their stage-I graphite intercalation compounds (GICs) were calculated and they are all found to be dynamically stable. Further, I simulated the APRI of those GICs with different densities and distribution way, which demonstrated that the sharp distinctions in APRI can be a clear and easy basis for identification of geometry and the crystallographic orientation.

ACKNOWLEDGEMENTS

The author thanks the Physical Research Platform (PRP) in School of Physics, SYSU.

DATA AVAILABILITY STATEMENT

The data that support the findings of this study are available from the corresponding author upon reasonable request.

NOTES AND REFERENCES

1. Conard J. Electronic structure of various forms of solid state carbons. Graphite intercalation compounds. New Trends in Intercalation Compounds for Energy Storage. Dordrecht: Springer; 2002.
2. Danzenbacher S, Molodtsov SL, Boysen J, Gantz T, Laubschat C, Shikin AM, et al. Electronic structure of graphite intercalation compounds of rare-earths and uranium. *Physica B-Condensed Matter*. 1999;259-61:1153-4. doi: 10.1016/s0921-4526(98)00610-3.
3. Pan ZH, Camacho J, Upton MH, Fedorov AV, Howard CA, Ellerby M, et al. Electronic Structure of Superconducting KC8 and Nonsuperconducting LiC6 Graphite Intercalation Compounds: Evidence for a Graphene-Sheet-Driven Superconducting State. *Phys Rev Lett*. 2011;106(18):4. doi: 10.1103/PhysRevLett.106.187002.
4. Klein HF, Nickl JJ, Besenhard JO, Gross J, Moehwald H. Graphite intercalation for permanent conductivity increase. Nickl J.
5. Wu JX, Mao NN, Xie LM, Xu H, Zhang J. Identifying the Crystalline Orientation of Black Phosphorus Using Angle-Resolved Polarized Raman Spectroscopy. *Angewandte Chemie-International Edition*. 2015;54(8):2366-9. doi: 10.1002/anie.201410108.
6. Zou B, Wei YD, Zhou Y, Ke DN, Zhang X, Zhang M, et al. Unambiguous determination of crystal orientation in black phosphorus by angle-resolved polarized Raman spectroscopy. *Nanoscale Horizons*. 2021;6(10):809-18. doi: 10.1039/d1nh00220a.
7. Yan K, Li Z, Wang W. Distinguishing different edge structures of graphene nanoribbons with Raman spectra, studied by first-principles calculations. *Journal of Raman Spectroscopy*. n/a(n/a). doi: <https://doi.org/10.1002/jrs.6336>.
8. Clancy AJ, Bayazit MK, Hodge SA, Skipper NT, Howard CA, Shaffer MSP. Charged Carbon Nanomaterials: Redox Chemistries of Fullerenes, Carbon Nanotubes, and Graphenes. *Chemical Reviews*. 2018;118(16):7363-408. doi: 10.1021/acs.chemrev.8b00128.
9. He CS, Wang WL. 2D Octagon-Structure Carbon and Its Polarization Resolved Raman Spectra. *Nanomaterials*. 2020;10(11). doi: 10.3390/nano10112252.
10. Deng ZX, Li ZB, Wang WL, She JC. Vibrational properties and Raman spectra of pristine and fluorinated blue phosphorene. *Physical Chemistry Chemical Physics*. 2019;21(3):1059-66. doi: 10.1039/c8cp05699d.
11. Shegai TO, Haran G. Probing the Raman scattering tensors of individual molecules. *Journal of Physical Chemistry B*. 2006;110(6):2459-61. doi: 10.1021/jp055750f.
12. Kranert C, Sturm C, Schmidt-Grund R, Grundmann M. Raman tensor elements of beta-Ga₂O₃. *Scientific Reports*. 2016;6. doi: 10.1038/srep35964.
13. Zheng W, Zheng RS, Huang F, Wu HL, Li FD. Raman tensor of AlN bulk single crystal. *Photonics Research*. 2015;3(2):38-43. doi: 10.1364/prj.3.000038.
14. Sander T, Eisermann S, Meyer BK, Klar PJ. Raman tensor elements of wurtzite ZnO. *Physical Review B*. 2012;85(16). doi: 10.1103/PhysRevB.85.165208.
15. Luo GF, Wang L, Li H, Qin R, Zhou J, Li LZ, et al. Polarized Nonresonant Raman Spectra of Graphene Nanoribbons. *Journal of Physical Chemistry C*. 2011;115(50):24463-8. doi: 10.1021/jp202870g.
16. Ceriotti M, Pietrucci F, Bernasconi M. Ab initio study of the vibrational properties of crystalline TeO₂: The alpha, beta, and gamma phases. *Physical Review B*. 2006;73(10):17. doi: 10.1103/PhysRevB.73.104304.
17. Liang LB, Meunier V. First-principles Raman spectra of MoS₂, WS₂ and their heterostructures. *Nanoscale*. 2014;6(10):5394-401. doi: 10.1039/c3nr06906k.
18. Umari P, Pasquarello A, Dal Corso A. Raman scattering intensities in alpha-quartz: A first-principles investigation. *Physical*

Review B. 2001;63(9):9. doi: 10.1103/PhysRevB.63.094305.

19. Zhang YJ, He X, Sun ML, Wang J, Ghosez P. Switchable metal-to-half-metal transition at the semi-hydrogenated graphene/ferroelectric interface. *Nanoscale*. 2020;12(8):5067-74. doi: 10.1039/c9nr08627g.

20. Hager JS, Zahardis J, Pagni RM, Compton RN, Li J. Raman under nitrogen. The high-resolution Raman spectroscopy of crystalline uranocene, thorocene, and ferrocene. *The Journal of Chemical Physics*. 2004;120(6):2708-18. doi: 10.1063/1.1637586.

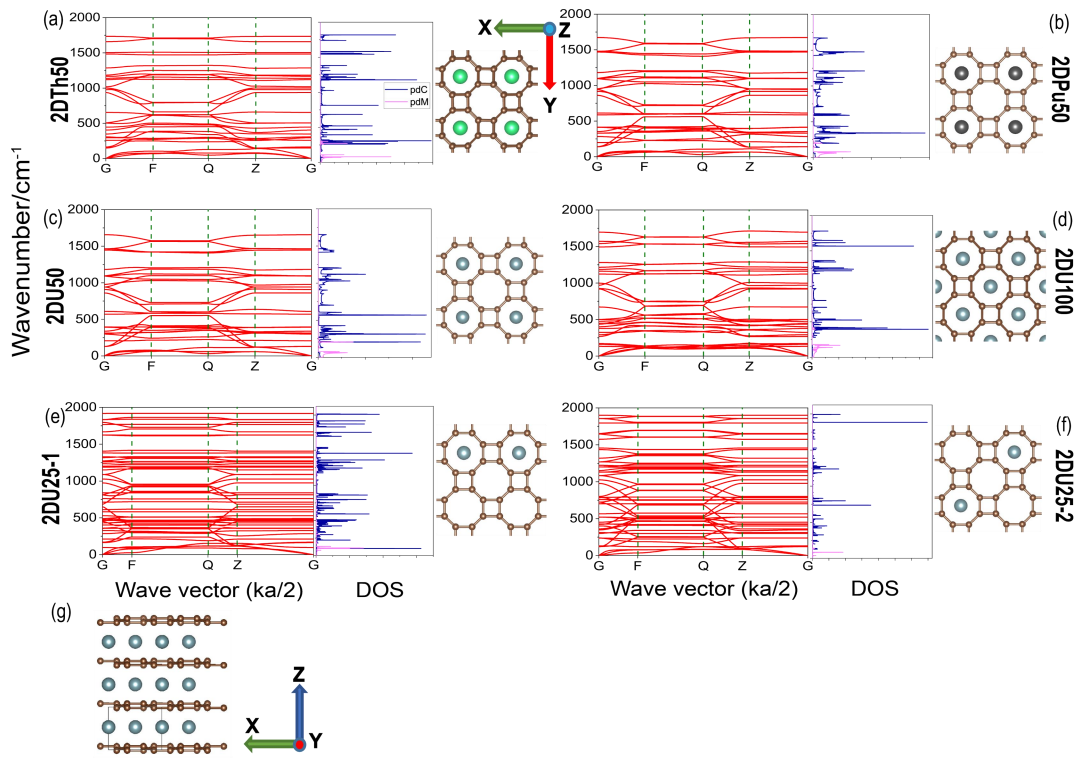


Fig.1 Phonon dispersion (left panels), phonon projected density of states (PDOS) (middle panels) and structural diagram viewed along Z-axis (right panels) of GICs with (a) Th (50%), (b) Pu (50%), (c) U (50%), (d) U (100%), (e) U (25%-1) and (f) U (25%-2). In the PDOS panels, pink curves are PDOS of metal elements and blue ones are that of carbons. In the structural diagrams, green balls are Th atoms, black ones are Pu, blue ones are U and brown ones are carbon. (g) structural diagram of 2DU100 viewed along Y-axis.

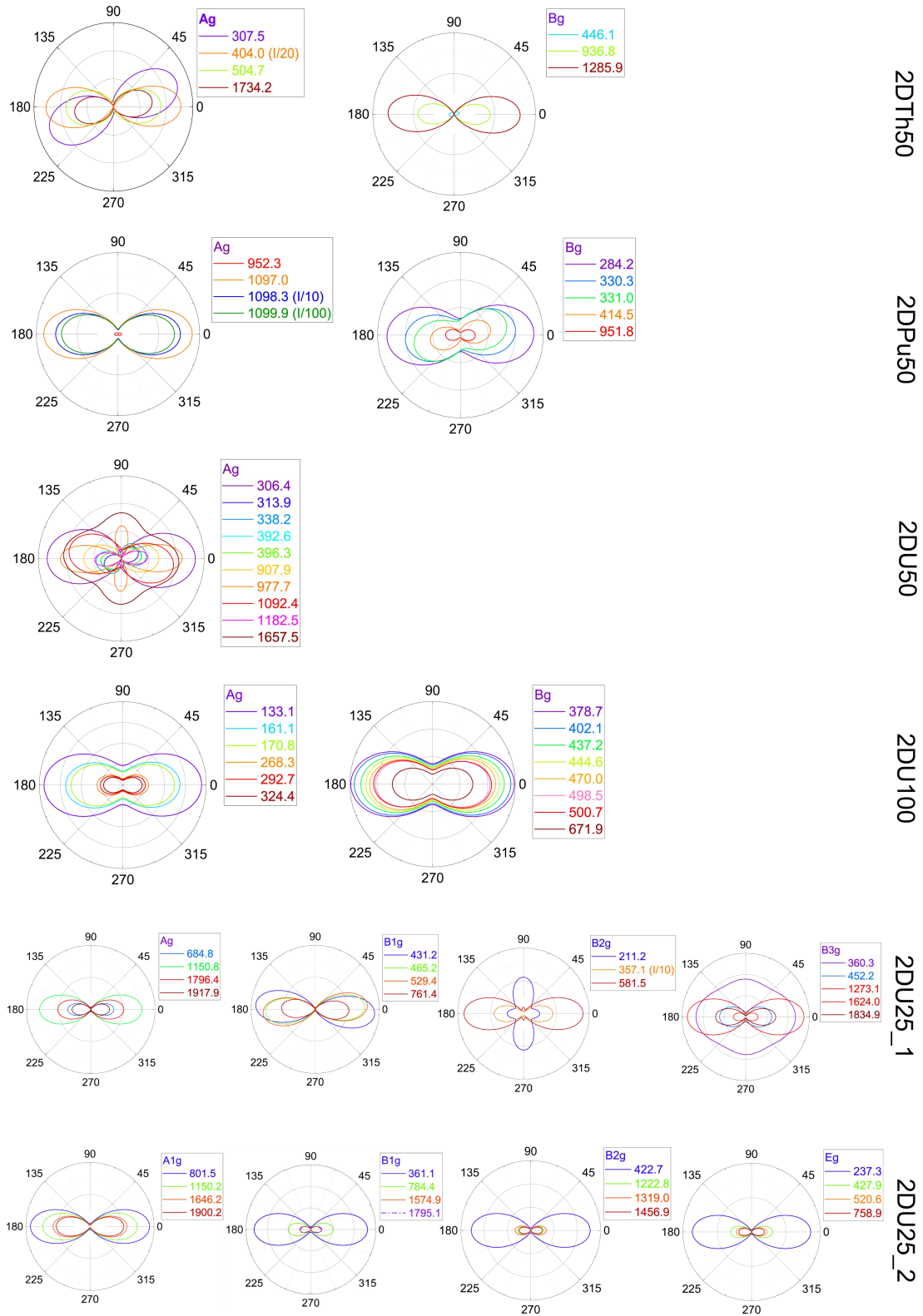


Fig. 2 Angle-resolved polarized Raman spectroscopy (APRS) of 6 types GICs with 633 nm laser incident along y-axis ($\hat{k}_i \parallel y$). The scattered light employs a parallel-polarization configuration ($\vec{e}_s \parallel \vec{e}_i$).

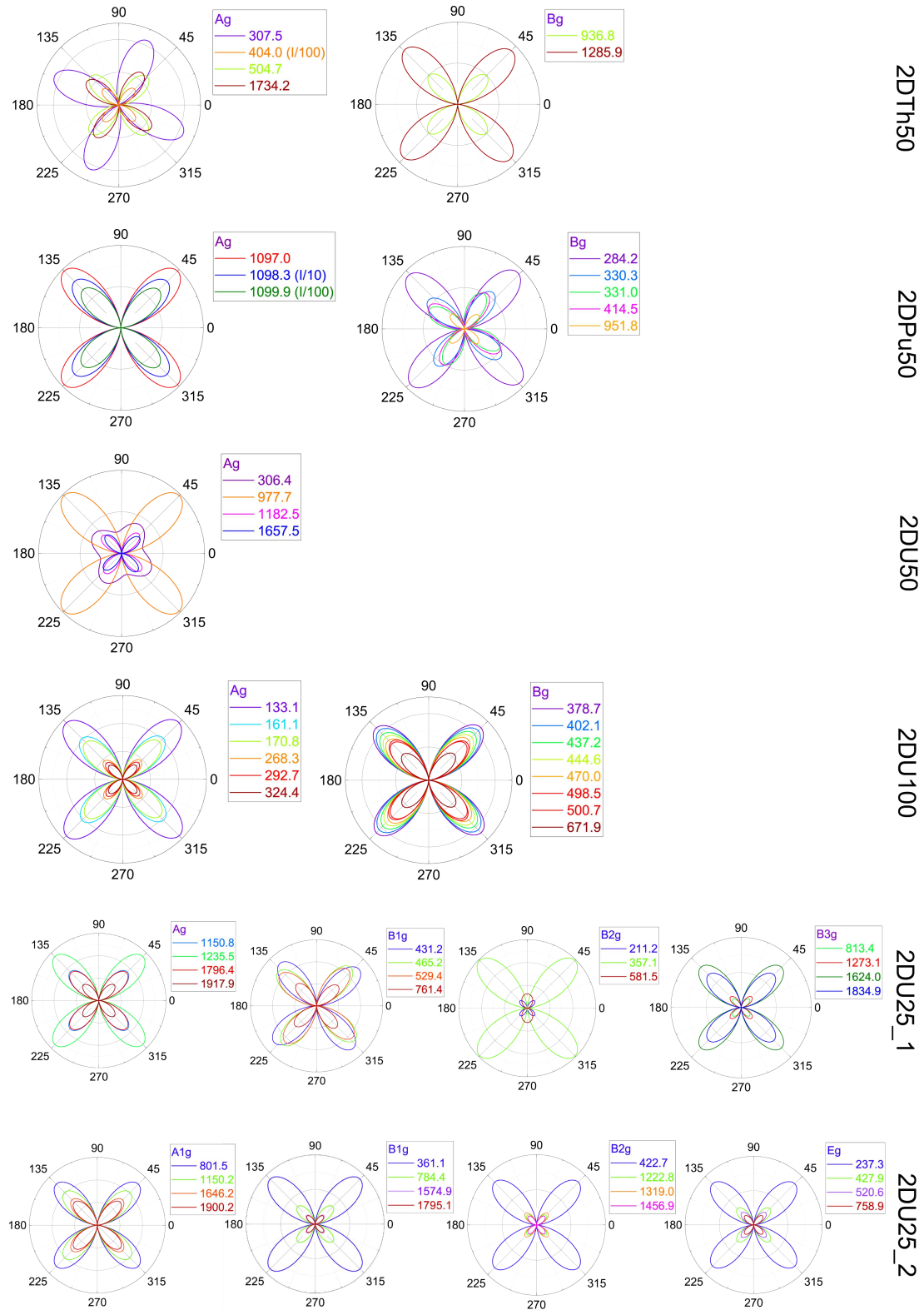


Fig. 3 Angle-resolved polarized Raman spectroscopy (APRS) of 6 types GICs with 633 nm laser incident along y-axis ($\hat{k}_i \parallel y$). The scattered light employs a cross-polarization configuration ($\vec{e}_s \perp \vec{e}_i$).

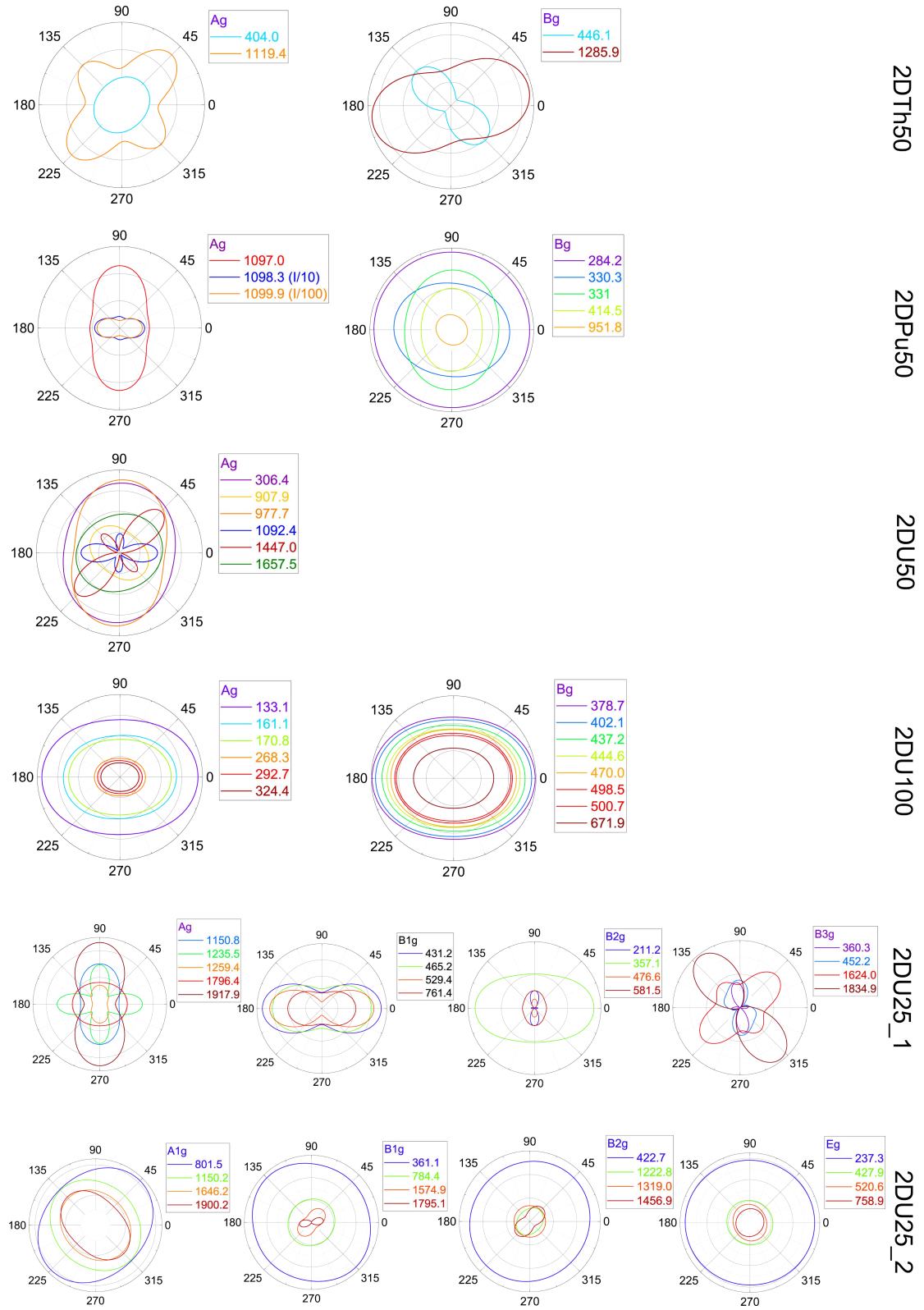


Fig. 4 Angle-resolved polarized Raman spectroscopy (APRS) of 6 types GICs with 633 nm laser incident along y-axis ($\hat{k}_i \parallel z$). The scattered light employs a parallel-polarization configuration ($\vec{e}_s \parallel \vec{e}_i$).

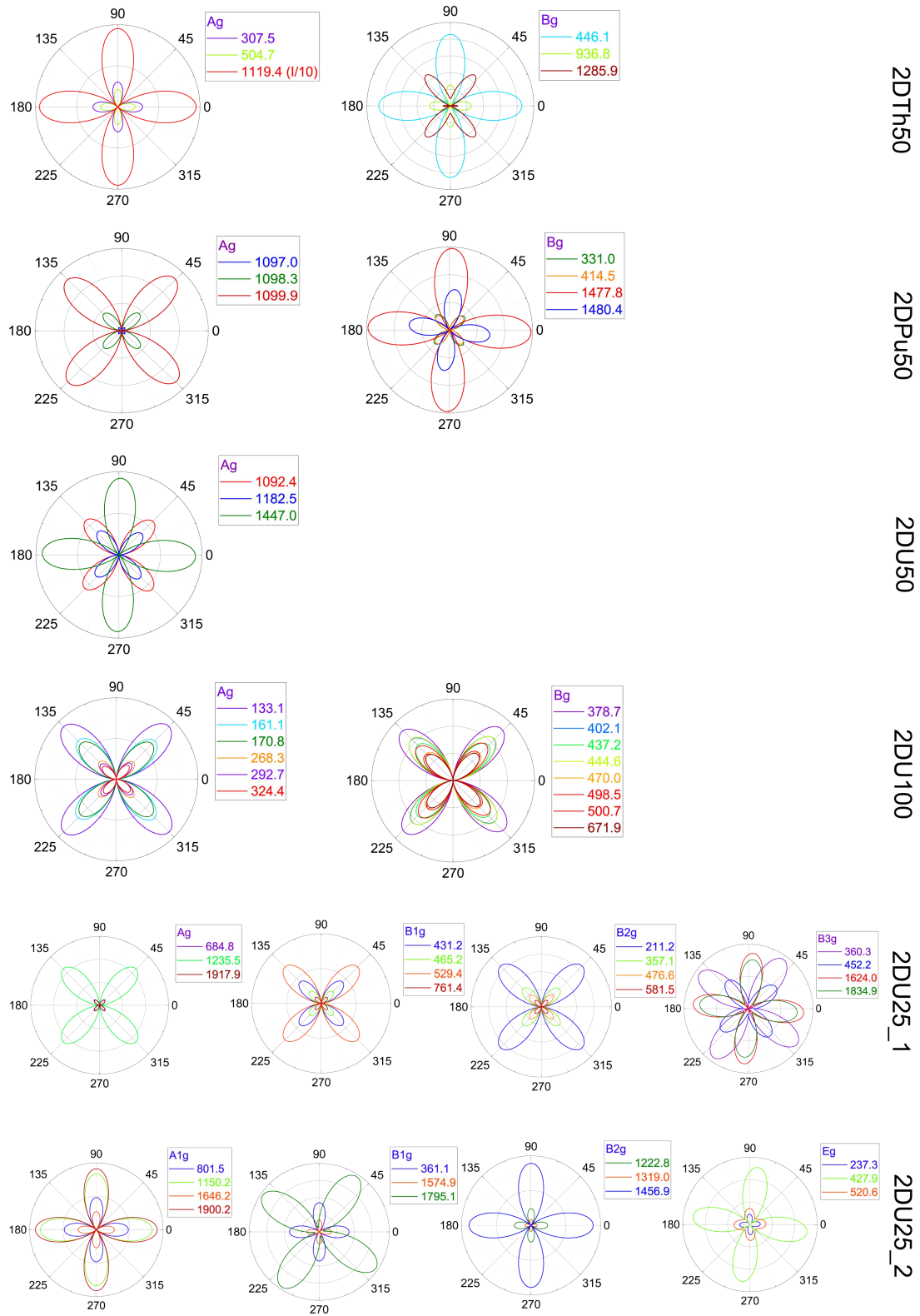
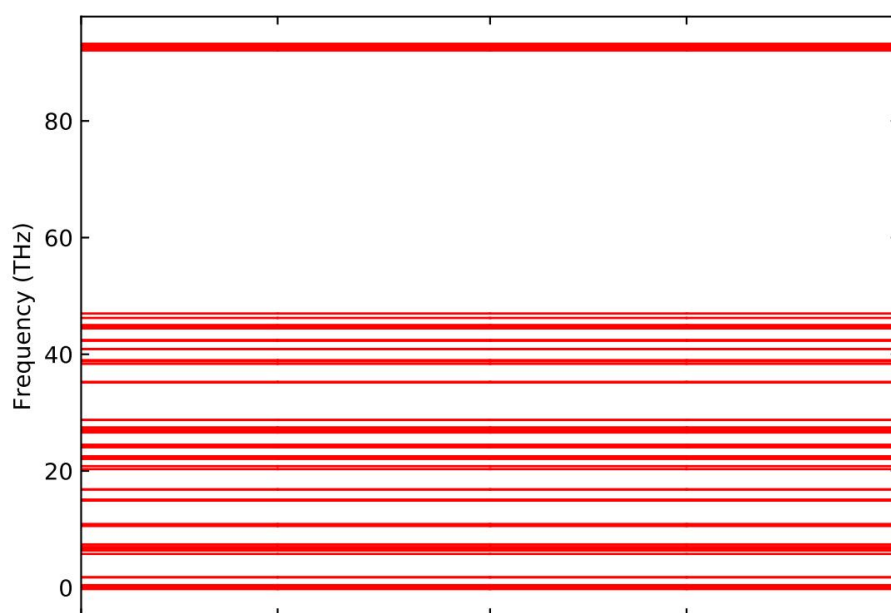


Fig. 5 Angle-resolved polarized Raman spectroscopy (APRS) of 6 types GICs with 633 nm laser incident along y-axis ($\hat{k}_i \parallel z$). The scattered light employs a parallel-polarization configuration ($\vec{e}_s \perp \vec{e}_i$).

Table 1. The Point group, Raman active modes and relative functions of the designed Organometallics

OM name	Point Group	Raman Active Modes	functions
2DUTh50	$C_{2h}(2/m)$	A_g	x^2, y^2, z^2, xy, Jz
		B_g	xz, yz, Jx, Jy
2DPu50	$D_{4h}(4/mmm)$	A_{1g}	x^2+y^2, z^2
		B_{1g}	x^2-y^2
2DU50	$D_{4h}(4/mmm)$	A_{1g}	x^2+y^2, z^2
2DU100	$C_{2h}(2/m)$	A_g	x^2, y^2, z^2, xy, Jz
		B_g	xz, yz, Jx, Jy
2DU25_1	$D_{2h}(mmm)$	A_g	x^2, y^2, z^2
		B_{1g}	xy, Jz
		B_{2g}	xz, Jy
		B_{3g}	yz, Jx
2DU25_2	$D_{4h}(4/mmm)$	A_{1g}	x^2+y^2, z^2
		B_{1g}	$x^2-y^2,$
		B_{2g}	xy
		E_g	$(xz, yz), (Jx, Jy)$



* BAND= 0.000 0.000 0.000 0.000 0.500 0.000 0.000 0.500 0.500
0.000 0.000 0.500 0.000 0.000 0.000

Fig. S1 Phonon spectrum of uranocene (calculated by GGA+U).

Table S1 Phonon frequencies calculated by GGA+U in this work (right table). They are closer to the experimental (RUN) data than the DFT results in the literature[20] (left table). The deviation may stem/come from the ignorance of vdW correction.

TABLE II. The observed RUN and calculated DFT Raman frequencies of $\text{Th}(\text{C}_8\text{H}_8)_2$, $\text{U}(\text{C}_8\text{H}_8)_2$, and $\text{C}_8\text{H}_8^{2-}$ ion with D_{8h} symmetry.

Mode	$\text{C}_8\text{H}_8^{2-}$		$\text{U}(\text{C}_8\text{H}_8)_2$		$\text{Th}(\text{C}_8\text{H}_8)_2$		Results of this work		
	DFT	RUN	DFT	RUN	DFT	RUN	U (C8H8) 2 no +U	DFT+U	Th (C8H8) 2 no +U
A_{1g}		212.05	215	222.0	219	219	216.9	212.5	217.0
	722	752.5	735	750.3	709	742	752.4	750.7	750.2
	2968	3041.1	3069	3042.2	3122		3065.2	3072.3	3064.6
E_{1g}		236.2	237	241.7	206	206	237.3	231.5	242.8
	595	725.62	774	722.1	750	750	740.5	694.4	734.6
			918		899				
E_{2g}		3168.7	1439	3020.7	1421	1421	3108.8	3109.5	3064.6
			3055		3103				255.2
			235	263.7	253	253	366.2	362.9	368.4
E_{2g}	325	379.86	378	386.8	364	364	897.6	897.1	892.4
		896.56	852	893.2	828	828	1155.7	1172.9	
	1127	1143.34	1194		1163		1498.8	1500.2	1492.5
	1452	1499.72	1520	1497.8	1496	1496	3065.2	3072.3	3064.6
	2899	3014.3	3042	2981.6	3091				

J. Chem. Phys., Vol. 120, No. 6 (2004)